Memory-Enhanced Plasticity Modeling of Sand Behavior under Undrained Cyclic Loading

Liu, H.; Diambra, Andrea ; Abell, José Antonio ; Pisano, F.

DOI
10.1061/(ASCE)GT.1943-5606.0002362

Publication date
2020

Document Version
Accepted author manuscript

Published in
Journal of Geotechnical and Geoenvironmental Engineering

Memory-enhanced plasticity modelling of sand behaviour under undrained cyclic loading

Haoyuan Liu[1], Andrea Diambra[2], José Antonio Abell[3], and Federico Pisanò[4]

[1]Norwegian Geotechnical Institute, Norway; Faculty of Civil Engineering and Geosciences, Delft University of Technology, The Netherlands.

[2]Department of Civil Engineering, Faculty of Engineering, University of Bristol, United Kingdom.

[3]Facultad de Ingeniería y Ciencias Aplicadas, Universidad de los Andes, Chile.

[4]Faculty of Civil Engineering and Geosciences, Delft University of Technology, The Netherlands. Email: F.Pisano@tudelft.nl

ABSTRACT

This work presents a critical state plasticity model for predicting the response of sands to cyclic loading. The well-known bounding surface SANISAND framework by Dafalias and Manzari (2004) is enhanced with a 'memory surface' to capture micro-mechanical, fabric-related processes directly effecting cyclic sand behaviour. The resulting model, SANISAND-MS, was recently proposed by Liu et al. (2019), and successfully applied to the simulation of drained sand ratcheting under thousands of loading cycles. Herein, novel ingredients are embedded into Liu et al. (2019)'s formulation to better capture the effects of fabric evolution history on sand stiffness and dilatancy. The new features enable remarkable accuracy in simulating undrained pore pressure build-up and cyclic mobility behaviour in medium-dense/dense sand. The performance of the upgraded SANISAND-MS is validated against experimental test results from the literature — including undrained cyclic triaxial tests at varying cyclic loading conditions and pre-cyclic consolidation histories. The proposed modelling platform will positively impact the study of relevant cyclic/dynamic problems, for instance, in the fields of earthquake and offshore geotechnics.

INTRODUCTION

Geotechnical structures subjected to cyclic loading may experience severe damage, or even failure, due to the soil losing its shear strength and stiffness, or experiencing excessive deformation under numerous loading cycles (Andersen 2009). Sound engineering analysis of these geotechnical systems must rely on accurate simulation of cyclic soil behaviour. This is to be pursued by means of constitutive models capable of reproducing a number of fundamental features of soil response under cyclic loading, such as irreversible/plastic straining (Youd 1993; Vaid and Thomas 1995), cyclic hysteresis (Berrill and Davis 1985; Kokusho 2013) and pore water pressure build-up (Seed and Rahman 1978; Berrill and Davis 1985; Ishihara 1993; Kokusho 2013) under a wide range of initial/boundary/drainage conditions.

In the past decades, a plethora of constitutive models – from very simple to highly sophisticated – have been proposed to reproduce cyclic soil behaviour in engineering applications. The case of sandy soils attracted particular attention after catastrophic geotechnical failures during seismic events (Ishihara 1993). The families of multi-surface (Prévost 1985; Elgamal et al. 2003; Houlsby and Mortara 2004) and bounding-surface (Dafalias and Popov 1975; Manzari and Dafalias 1997; Papadimitriou and Bouckovalas 2002; Pisanò and Jeremić 2014) plasticity models have proven successful in capturing relevant features of cyclic sand behaviour. Special mention in this context goes to the SANISAND04 model proposed by Dafalias and Manzari (2004), built on Manzari and Dafalias (1997) and forefather of several later formulations (Zhang and Wang 2012; Boulanger and Ziotopoulou 2013; Dafalias and Taiebat 2016; Petalas et al. 2019). Among these, the PM4Sand model (Boulanger and Ziotopoulou 2013; Ziotopoulou and Boulanger 2016) possesses remarkable capabilities to reproduce undrained cyclic behaviour, including the simulation of pore pressure build-up, liquefaction triggering and, in medium-dense/dense sands, ‘cyclic mobility’ (Elgamal et al. 2003) – in turn associated with transient regains in shear resistance, and gradual shear strain accumulation at vanishing confinement. Cyclic mobility is relevant to the serviceability of earth structures and foundations under prolonged cyclic loading (Ziotopoulou and Boulanger 2016; Kementzetzidis et al. 2019), as well as to seismic site response (Roten et al. 2013).

Recently, Liu et al. (2019) enhanced the SANISAND04 formulation by introducing the concept of memory surface (MS) (Stallebrass and Taylor 1997; Maleki et al. 2009; Corti et al. 2016) to better account for fabric-related effects and their impact on cyclic ratcheting behaviour (Houlsby et al. 2017). The model – henceforth referred to as SANISAND-MS – can predict variations in soil stiffness and strain accumulation under thousands of drained loading cycles (high-cyclic loading). The same modelling features also allow better simulation of the undrained hydro-mechanical response, especially in terms of extent and timing of cyclic pore pressure accumulation (Liu et al. 2018). It was noted, however, that further improvements would be needed to unify the simulation of undrained cyclic behaviour over a wide range of initial sand densities and loading conditions (Liu et al. 2018).

This work takes further the success of SANISAND-MS as presented in Liu et al. (2019), with reference to undrained cyclic loading. Besides the ability of capturing liquefaction triggering, the emphasis of this work lies on the following aspects: (i) cyclic pore pressure build-up, including its cycle-by-cycle timing in the pre-liquefaction stage; (ii) stress-strain response in the post-liquefaction phase (cyclic mobility behaviour); and (iii) influence of previous loading history on the undrained cyclic response. These objectives are accomplished without compromising the previous achievements of Liu et al. (2019).

The performance of the upgraded SANISAND-MS formulation is inspected in detail, and thoroughly validated against the experimental datasets from Wichtmann (2005) and Wichtmann and Triantafyllidis (2016) – including undrained cyclic triaxial tests on both isotropically and anisotropically consolidated sand specimens. The present research is largely motivated by current offshore wind developments, where the need for advanced analysis of cyclic soil-foundation interaction is particularly felt (Pisanò 2019).

UPGRADED SANISAND-MS FORMULATION

Notation

Stresses are meant as 'effective' throughout the paper, bold-face notation is used for tensor quantities, and the symbol ':' stands for inner tensor product. Stresses and strains are represented by the tensors $\boldsymbol{\sigma}$ and $\boldsymbol{\varepsilon}$, with typical tensor decompositions including: deviatoric stress $\boldsymbol{s} = \boldsymbol{\sigma} - p\boldsymbol{I}$, with $p = \text{tr}\boldsymbol{\sigma}/3$ effective mean stress and $\boldsymbol{I}$ identity tensor; deviatoric strain $\boldsymbol{e} = \boldsymbol{\varepsilon} - (\varepsilon_{vol}/3)\boldsymbol{I}$, with $\varepsilon_{vol} = \text{tr}\boldsymbol{\varepsilon}$ volumetric strain – superscripts e and p are used to denote 'elastic' and 'plastic' strain components. The deviatoric stress ratio tensor is defined as $\boldsymbol{r} = \boldsymbol{s}/p$. The deviatoric stress q is defined as $q = \sqrt{3J_2}$, with J_2 second invariant of $\boldsymbol{s}$. The symbols 'tr' and '$\langle\rangle$' indicate trace and Macauley brackets operators, respectively.

Background

The proposed version of SANISAND-MS upgrades the formulation by Liu et al. (2019), built on the SANISAND04 bounding surface model (Dafalias and Manzari 2004) and enriched with the notion of memory surface (Corti et al. 2016), which replaces the fabric tensor of the original formulation. The general representation of all model loci in the normalised deviatoric stress ratio plane is provided in Fig.1. The model formulation is founded on the critical state theory and makes use of: (1) a narrow conical yield locus (f) enclosing the elastic domain; (2) a wide conical bounding surface (f^B), setting stress bounds compliant with an evolving state parameter Ψ (Been and Jefferies 1985) as per Manzari and Dafalias (1997); (3) a conical dilatancy surface (f^D), separating stress zones associated with contractive and dilative deformations as a function of Ψ (Manzari and Dafalias 1997; Li and Dafalias 2000; Dafalias and Manzari 2004); (4) a conical memory surface (f^M), bounding an evolving stress region related to increased hardening response due to 'non-virgin' loading and, in turn, stress-induced anisotropy at the micro-scale. The memory surface enables phenomenological representation of fabric changes induced by the cyclic loading history, such as variations in stiffness and dilatancy. The memory mechanism takes place in the multi-dimensional stress space and is intrinsically sensitive to the loading direction.

The model features non-associated plastic flow and, owing to the state parameter mechanism, is able to reproduce sand behaviour over a wide range of void ratios via a single set of parameters. Several modelling ingredients – e.g., elastic relationships, deviatoric plastic flow, critical state line (CSL) and model surfaces – are directly inherited from Liu et al. (2019). The use of the yield back-stress ratio $\boldsymbol{\alpha}$ is resumed here as in Dafalias and Manzari (2004) to avoid certain numerical inconveniences, so that its projections onto bounding, dilatancy and critical state surfaces are employed in the model formulation. For brevity, already published constitutive equations are only reported in Appendix A, while main focus is on defining and validating new model features.

New features

New relationships for memory surface evolution, plastic flow rules and hardening laws are presented in this section and summarised in Appendix A. The new model ingredients do not affect the capabilities of the previous formulation, but do influence the calibration of certain cyclic parameters inherited from Liu et al. (2019). Calibration and role of newly defined parameters are discussed in what follows. Ideally, four extra-tests would be needed for their calibration, including stress-controlled undrained cyclic triaxial tests at different relative densities and cyclic stress ratios. Nevertheless, the upgraded model can be reduced to a 'lighter' version whenever convenient.

The implications of the mentioned improvements are elucidated by comparing previous and latest SANISAND-MS simulations of triaxial test results from Wichtmann and Triantafyllidis (2016). The reference cyclic undrained tests were performed on Karlsruhe fine sand (D_{50} = $0.14mm$, $C_u = D_{60}/D_{10} = 1.5$, $e_{max} = 1.054$, $e_{min} = 0.677$). Simulations of the previous SANISAND-MS model (Liu et al. 2019) are related to the soil parameters given in Appendix A from Liu et al. (2018).

Memory surface and its evolution

The memory surface (f^M) tracks stress states already experienced by the sand during its (cyclic) loading history. It accounts for fabric changes and load-induced anisotropy via the evolution of its size (m^M) and back-stress ratio ($\boldsymbol{\alpha}^M$) (Corti et al. 2016; Liu et al. 2019; Liu and Pisanò 2019). The expansion of the memory surface (i.e., increase in m^M) corresponds to the experimental observation of sand becoming stiffer as fabric is reinforced by cycling within the 'non-virgin' domain. On the other hand, the occurrence of dilation causes loss of sand stiffness (Nemat-Nasser and Tobita 1982), which can be reproduced by the model through a decrease in m^M. This experimental evidence led to postulate a parallel shrinking mechanism for the memory surface, so that the change in memory surface size (dm^M) is decomposed into two terms: a memory surface expansion term dm_+^M and a memory surface contraction term dm_-^M :

$$dm^M = dm_+^M + dm_-^M \tag{1}$$

Enforcing plastic consistency under 'virgin loading' (i.e., with tangent yield and memory surfaces at the current stress point $\boldsymbol{\sigma}$ and the memory surface has no influence on soil stiffness, see Liu et al. (2019)) in the contractive regime allows to derive the (positive) expansion rate dm_+^M:

$$dm_+^M = \sqrt{3/2}d\boldsymbol{\alpha}^M : \boldsymbol{n} \tag{2}$$

where $\boldsymbol{n}$ is the unit tensor normal to the yield surface f (Fig.2a). As discussed in Liu et al. (2019), variations in size and location of the memory surface are inter-related. $d\boldsymbol{\alpha}^M$ describes the translation of the memory surface centre, assumed to take place along the direction of $\boldsymbol{\alpha}^b - \boldsymbol{r}_\alpha^M$:

$$d\boldsymbol{\alpha}^M = 2/3\langle L\rangle h^M(\boldsymbol{\alpha}^b - \boldsymbol{r}_\alpha^M) \tag{3}$$

in which $\boldsymbol{\alpha}^b$ is the bounding back-stress ratio (Fig.2a) and $\boldsymbol{r}_\alpha^M = \boldsymbol{\alpha}^M + \sqrt{2/3}(m^M - m)\boldsymbol{n}$ (different from the memory image point $\boldsymbol{r}^M = \boldsymbol{\alpha}^M + \sqrt{2/3}m^M\boldsymbol{n}$ in Fig.1). L is the plastic multiplier (Appendix A), while h^M is the counterpart of the hardening coefficient defined with respect to the memory surface — its expression is specified later on.

As a new feature, the shrinkage rate of the memory surface dm_-^M is further linked to the induced cumulative expansion of the memory surface size $m_+^M = \int dm_+^M$ over the whole loading history experienced from a known initial state. The introduction of the term m_+^M, monotonically increasing under shearing and consequent plastic straining, ensures rapid degradation of the memory surface at large strain levels. Therefore, virgin loading conditions are quickly reinstated upon load increment reversal after severe dilation (due to inhibited memory surface effects). This feature is consistent with the observations of Yimsiri and Soga (2010) and Ziotopoulou and Boulanger (2016), who noted that sand behaviour at large strain levels is mainly governed by the current relative density:

$$dm_{-}^{M} = -\frac{m^{M}}{\zeta} f_{shr} \langle b_r^b \rangle m_{+}^{M} \left\langle -d\varepsilon_{vol}^{p} \right\rangle \tag{4}$$

where ζ is a parameter governing the shrinking rate of the memory surface, while the geometrical factor f_{shr} ensures that the memory surface never becomes smaller than the elastic domain (see Appendix 1 in Liu et al. (2019) for details):

$$f_{shr} = 1 - (x_1 + x_2)/x_3 \tag{5}$$

with $x_{1,2,3}$ illustrated in Fig.2b and defined as:

$$\begin{aligned} x_1 &= \boldsymbol{n}^M : (\boldsymbol{r}^M - \boldsymbol{r}) \\ x_2 &= \boldsymbol{n}^M : (\boldsymbol{r} - \tilde{\boldsymbol{r}}) \\ x_3 &= \boldsymbol{n}^M : (\boldsymbol{r}^M - \tilde{\boldsymbol{r}}^M) \end{aligned} \tag{6}$$

In Eq.6:

$$\tilde{\boldsymbol{r}} = \boldsymbol{\alpha} - \sqrt{2/3} m \boldsymbol{n} \qquad \tilde{\boldsymbol{r}}^M = \boldsymbol{\alpha}^M - \sqrt{2/3} m^M \boldsymbol{n} \tag{7}$$

and $\boldsymbol{n}^M$ is the unit tensor oriented parallel to $(\boldsymbol{r}^M - \boldsymbol{r})$ (see Fig.2b):

$$\boldsymbol{n}^M = (\boldsymbol{r}^M - \boldsymbol{r}) / \sqrt{(\boldsymbol{r}^M - \boldsymbol{r}) : (\boldsymbol{r}^M - \boldsymbol{r})} \tag{8}$$

The term $< b_r^b >$ in Eq.4 is also introduced to properly handle strain-softening stages: during strain softening, $(\boldsymbol{\alpha}^b - \boldsymbol{\alpha}) : \boldsymbol{n} < 0$, which may results in $b_r^b = (\boldsymbol{\alpha}^b - \boldsymbol{r}_{\alpha}^M) : \boldsymbol{n} < 0$ and contemporary shrinkage of both bounding and memory surfaces may occur. As a consequence, $dm_{+}^{M} < 0$ and m_{+}^{M} may decrease, which would be in contrast with the assumption of non-decreasing m_{+}^{M}.

The following expression of the memory surface hardening coefficient h^M in Eqs. 2–3 results from derivations similar to those in Liu et al. (2019) (see Table 1):

$$h^M = \frac{1}{2}\left(\tilde{h} + \hat{h}\right) = \frac{1}{2}\left[\frac{b_0}{(\boldsymbol{r}_\alpha^M - \boldsymbol{\alpha}_{in}) : \boldsymbol{n}} + \sqrt{\frac{3}{2}}\frac{m^M m_+^M f_{shr}\langle b_r^b\rangle \langle -D\rangle}{\zeta(\boldsymbol{\alpha}^b - \boldsymbol{r}_\alpha^M) : \boldsymbol{n}}\right] \tag{9}$$

where b_0 is the hardening factor given by Dafalias and Manzari (2004) (Appendix A), and $\boldsymbol{\alpha}_{in}$ the back-stress ratio at stress increment reversal. Closer inspection of Eq. 9 leads to recognise the chance of a vanishing denominator in $\hat{h}$ (e.g., if either $\boldsymbol{\alpha}^b = \boldsymbol{r}_\alpha^M$ or $\boldsymbol{n} \perp (\boldsymbol{\alpha}^b - \boldsymbol{r}_\alpha^M)$), which may abruptly accelerate the evolution of $\boldsymbol{\alpha}^M$ and temporarily leave the yield locus outside the (shrinking) memory surface. The effects of such occurrence, rare but possible, may be mitigated in the numerical implementation of the model, for instance by inhibiting shrinkage of the memory surface when becoming tangent to the yield surface.

Overall, the above upgraded laws for memory surface evolution allow to erase fabric effects at large strain levels, in agreement with available experimental evidence (Yimsiri and Soga 2010; Ziotopoulou and Boulanger 2016).

Dilatancy

The model proposed by Liu et al. (2019) can already predict liquefaction triggering (according to Seed and Lee (1966), the first occurrence of $p' \approx 0$), and provides for medium-dense/dense sands reasonable stress path shapes in the post-dilation phase ('butterfly-shaped' $q - p$ response). However, accurate simulation of peculiar stress-strain loops during cyclic mobility is beyond the possibilities of that model. Ammending this short-coming requires introducing changes to the formulation governing sand dilatancy. Indeed, as discussed by Elgamal et al. (2003) and Boulanger and Ziotopoulou (2013), the modelling of cyclic mobility is intimately related to the description of sand dilatancy. Within the SANISAND framework, the dilatancy coefficient D in the plastic flow rule is generally expressed as (Appendix A):

$$D = A_d d \tag{10}$$

where

$$d = (\boldsymbol{\alpha}^d - \boldsymbol{\alpha}) : \boldsymbol{n} \tag{11}$$

and $\boldsymbol{\alpha}^d$ represents the image back-stress ratio on the dilatancy surface. In Liu et al. (2019), the term A_d was already set to depend on the sign of plastic volume changes (i.e., contraction or dilation) before the previous load increment reversal through the term $\langle \tilde{b}_d^M \rangle = \langle (\tilde{\boldsymbol{\alpha}}^d - \tilde{\boldsymbol{r}}_\alpha^M) : \boldsymbol{n} \rangle$. Such a dependence was introduced to capture the increase in pressure build-up upon post-dilation load increment reversals — a phenomenon that Dafalias and Manzari (2004) reproduced through the concept of fabric tensor. Compared to Liu et al. (2019), the definition of A_d is here enhanced with some new features, mainly instrumental to the simulation of undrained cyclic mobility:

– in case of (plastic) contraction ($d \geq 0$) following previous contraction ($\tilde{b}_d^M \leq 0$):

$$A_d = A_0 \tag{12}$$

– in case of (plastic) contraction ($d \geq 0$) following previous dilation ($\tilde{b}_d^M > 0$)

$$A_d = A_0 \exp\left[\beta_1 F \left(\frac{p}{p_{max}}\right)^{0.5}\right] g^k(\theta) \tag{13}$$

– in case of dilation ($d < 0$)

$$A_d = A_0 \exp\left[\beta_2 F \left(1 - \left(\frac{p}{p_{max}}\right)^{0.5}\right) \frac{d}{||\boldsymbol{\alpha}^c||}\right] \frac{1}{g(\theta)} \tag{14}$$

In the above relationships, A_0 is the 'intrinsic' dilatancy parameter already present in Dafalias and Manzari (2004). $||\boldsymbol{\alpha}^c||$ in Eq.14 is the Euclidean norm of $\boldsymbol{\alpha}^c$ (see Appendix A) introduced for normalisation purposes, which represents the distance between the origin of the deviatoric stress ratio plane and the image back-stress ratio on the critical surface f^C (Fig.1). The new dilatancy features in Eqs.13-14 are phenomenologically associated with the following mechanical factors:

- **Fabric history**

F is a non-decreasing scalar variable related to the previous history of fabric evolution:

$$F = \ln\left[1 + \frac{|m_-^M|}{(|m_+^M| + |m_-^M|)^{0.5}}\right] = \ln\left[1 + \frac{\int |dm_-^M|}{(\int |dm_+^M| + \int |dm_-^M|)^{0.5}}\right] \tag{15}$$

F plays a similar role as the 'damage index' in Boulanger and Ziotopoulou (2013), that is to progressively degrade A_d at increasing number of cycles. This feature helps reproducing progressive shear strain accumulation, for instance in undrained DSS tests with imposed symmetric shear loading (Arulmoli et al. 1992; Andersen 2009). The effect of this modelling ingredient can be appreciated by comparing model simulations in Fig.3a and Fig.3b, performed with previous and upgraded SANISAND-MS, respectively. It should also be noted that, as F is a non-decreasing variable, it will permanently have an influence also on the post-cyclic response, possibly featuring different drainage conditions. Post-cyclic drained behaviour, for instance, would be more (less) contractive (dilative) than without the use of F in the flow rule. There is hardly any experimental evidence available to either support or falsify such occurrence, so that caution is recommended when applying the model to problems with very variable drainage conditions and/or distinct stages of consolidation.

- **Sensitiveness to stress state and path**

  Dependence on the (relative) Lode angle function ($g(\theta)$) and the term $d/||\boldsymbol{\alpha}^c||$ were suggested by experimental results as a way to modulate the response, and particularly strain accumulation, with respect to different cyclic stress paths (e.g., triaxial or simple shear). Typical simulation results of previous and upgraded SANISAND-MS models are shown in Figs.4a and 4b, respectively. The pressure term $(p/p_{max})^{0.5}$ (p_{max} is the highest effective mean pressure ever experienced) reflects the higher proneness to shear straining observed at very low effective stress levels, progressively reducing at increasing p – see Fig.3b and Fig.4b.

Dilatancy features in the upgraded model can be tuned to experimental data through the material parameters β_1 and β_2 in Eqs.13 and 14. These parameters govern cyclic shear straining in the dilative regime – cyclic volume changes before any dilation mostly depend on the parameter A_0 and the memory-hardening parameter μ_0 in Appendix A. Sound calibration of β_1 requires data from undrained cyclic triaxial tests in which initial liquefaction is triggered. As exemplified in Fig.5, the parameter β_1 influences the undrained triaxial stress-strain response in terms of ultimate normalised accumulated pore pressure (throughout this work, pore water pressure generation is tracked at the end of each full cycle when $q = q_{ave}$ level). Larger β_1 results in higher u^{acc}/p_{in} ratios (i.e., smaller residual effective stress). For the considered Karlsruhe fine sand $\beta_1 = 4$ was selected, with β_2 negligibly affecting the final u^{acc} level.

At given β_1, increasing β_2 results in larger accumulation of cyclic shear strain in undrained cyclic DSS tests (see Fig.3b). Unfortunately, in the lack of undrained cyclic DSS tests performed on the same Karlsruhe sand, β_2 had to be identified, together with k in Eq.13, by a trial-and-error procedure. In the case of triaxial loading, increasing β_2 determines larger cyclic axial strain (see Fig.6b), whereas the parameter k in Eq.13 governs the influence of the stress path through the relative Lode angle θ in Fig.1. Fig.6b shows that, for a cyclic triaxial test, higher k results in positive/compressive cyclic axial strains larger than on the negative/extension side. The comparison to Wichtmann and Triantafyllidis (2016)'s triaxial test results (Fig.6a) led to identify the parameter pair $\beta_2 = 3.2$ and $k = 2$. Two remarks about formulation and limitations of the new flow rule:

1. The piece-wise definition of A_d implies discontinuity in the dilatancy coefficient D when the material transits from contractive to dilative behaviour (i.e., when the yield locus crosses the dilatancy surface) – even in presence of continuous variations in stress ratio $\boldsymbol{r}$ (thus, in loading direction $\boldsymbol{n}$). Consequently, continuity of volumetric plastic strain increments may not be guaranteed, similarly to Boulanger and Ziotopoulou (2013) and Khosravifar et al. (2018);
2. In contrast with the (inconclusive) findings of some experimental studies, the model predicts unlimited strain accumulation during cyclic mobility – compare to Fig.6a, where only limited strain increments are observed in the last few loading cycles. While other modelling assumptions are certainly possible (Barrero et al. 2019), the latter point will receive further

attention when broader consensus about underlying physical mechanisms is reached (Wang and Wei 2016; Wang et al. 2016).

Hardening coefficient

In its first version, SANISAND-MS had limited capability to quantitatively reproduce complex relationships between cyclic pore pressure accumulation and relevant loading factors. Fig.7 compares the performance of previous SANISAND-MS (blue lines) (Liu et al. 2019) in reproducing Wichtmann and Triantafyllidis (2016)'s triaxial data (blacks lines) regarding undrained pre-liquefaction behaviour under cyclic symmetric loading at varying cyclic amplitude ratios ($\eta_{ampl} = q_{ampl}/p_{in}$, with q_{ampl} the cyclic shear amplitude and p_{in} the initial mean effective stress). The previous SANISAND-MS predicts more limited variation in the number of loading cycles N_{ini} to trigger initial liquefaction ($u^{acc}/p_{in} \approx 1$ for the first time).

The comprehensive database of Wichtmann and Triantafyllidis (2016) supports the idea that more cycles are required to trigger liquefaction (higher N_{ini}) at low η_{ampl}. It could thus be attempted to link the increase in N_{ini} to higher values of the hardening coefficient h through explicit dependence on η_{ampl}. However, as η_{ampl} cannot be a priory defined in general boundary value problems, the current stress ratio η instead of η_{ampl} is adopted in the upgraded definition of the hardening coefficient h:

$$h = \frac{b_0}{(\boldsymbol{\alpha} - \boldsymbol{\alpha}_{in}) : \boldsymbol{n}} \exp\left[\mu_0 \left(\frac{p}{p_{atm}}\right)^{0.5} \left(\frac{b^M}{b_{ref}}\right)^{w_1} \frac{1}{\eta^{w_2}}\right] \tag{16}$$

where $\eta = q/p = \sqrt{3J_2}/p$ (see *Notation* section). b^M represents the distance between the current back-stress ratio $\boldsymbol{\alpha}$ and its image point $\boldsymbol{r}_\alpha^M$ on the memory surface, while b_{ref} is a reference normalisation factor (Appendix A). The term $1/\eta^{w_2}$ (with w_2 new model parameter), explicitly accounts for the deviatoric span of the loading path – for more robust numerical implementation, m (radius of the yield surface in the stress ratio π plane) is set as η's lower bound.

Input to the calibration of the w_2 parameter can be obtained from the experimental relationship between N_{ini} and η_{ampl} in triaxial tests on isotropically consolidated sand. As mentioned above, increase in N_{ini} is linked to higher values of the hardening coefficient h, which is in turn inversely related to η_{ampl} (i.e., $N_{ini} \propto h \propto [\exp(\text{factor} \cdot 1/\eta_{ampl}^{w_2})]$). Such observation prompted the investigation of the relationship between $\ln(N_{ini})$ and $1/\eta_{ampl}^{w_2})$. It was concluded that for fixed η_{ampl}, dense sands (i.e., with D_{r0} larger than critical) experience more loading cycles before liquefaction. In summary, the experimental relationship between $\ln(N_{ini})/D_{r0}$ and $1/(\eta_{ampl}^{w_2})$ emerging from a set of tests is proposed as a tool to calibrate w_2 – see Fig.8. This requires at least four stress-controlled undrained triaxial tests on isotropically consolidated specimens, at varying η_{ampl} and D_{r0}, until cyclic liquefaction is triggered. However, since in Eq.16 the current stress ratio η is adopted instead of directly using η_{ampl}, the calibrated w_2 may need further adjustment together with w_1 and μ_0 (for which calibration procedures are given in the following section). Should available data be insufficient, $w_2 = 0$ is suggested as an initial value, and followed with a sensitivity study to determine its relevance and possibly motivate the gathering of the data for its calibration.

The other exponent w_1 in Eq.16 was pre-set to 2 in Liu et al. (2019) for simplicity. Herein, w_1 is re-activated as a free model parameter for more flexibility. Its value, together with μ_0's, was calibrated mostly by trial-and-error, starting from the default setting $w_1 = 2$. The same test data-set used for calibrating w_2 can also support the identification of w_1 when looking at pore pressure accumulation trends, e.g., in terms of u^{acc}/p_{in} versus number of loading cycles. Fig.9 shows that good agreement for the examined Karlsruhe sand is achieved for $\mu_0 = 65$ and $w_1 = 2.5$.

Fig.7 also shows the performance of upgraded SANISAND-MS (red lines). As discussed in the following section, the upgraded model appears better suited to capture the dependence of N_{ini} (number of cycles to liquefaction) on the cyclic stress amplitude at different relative densities.

PREDICTION OF UNDRAINED CYCLIC RESPONSE

This section demonstrates the predictive capabilities of the model with respect to undrained cyclic loading. Using the set of calibrated parameters in Table 3, the model performance is assessed against additional triaxial test results on Karlsruhe fine sand (Wichtmann and Triantafyllidis 2016), not previously used for calibration.

Response of isotropically consolidated sand

Cyclic pore pressure accumulation

Cyclic build-up of pore pressure may cause stiffness and strength losses (cyclic liquefaction), for instance during seismic events. Many empirical models have been developed (Dobry et al. 1985; Idriss and Boulanger 2006; Ivšić 2006; Chiaradonna et al. 2018) to simplify the prediction of such build-up by directly relating the pore pressure ratio (u^{acc}/p_{in}) to the ratio between current number of cycles (N) and total number of cycles to liquefaction (N_{ini}). It seems interesting to verify how pore pressure predictions from SANISAND-MS (both previous and upgraded versions) compare to empirical models, such as that recently proposed by Chiaradonna et al. (2018). In Fig.10, SANISAND-MS and empirical model predictions are compared to experimental data from Wichtmann and Triantafyllidis (2016), concerning triaxial tests performed at varying cyclic stress amplitude ratio. Although both plasticity and empirical models reproduce well experimental data, it is worth noting that the simulation of pore pressure accumulation trends is usually easier when pursued in terms of normalised number of cycles N/N_{ini}. It is shown hereafter that reproducing the absolute N_{ini} value poses a more serious challenge for constitutive modelling.

Influence of initial effective mean pressure Experimental test results from Wichtmann and Triantafyllidis (2016) (Fig.11) show that it is not straightforward to interpret the influence of the initial consolidation pressure p_{in} in tests featuring constant cyclic stress amplitude ratio ($\eta_{ampl} = q_{ampl}/p_{in}$). Axial strain accumulation in the cyclic mobility stage does not show obvious dependence on p_{in} either. Simulation results obtained with the upgraded SANISAND-MS formulation support similar conclusions (Fig.11b). For instance, the considered cases with $\eta_{ampl} = 0.25$ and p_{in} =100, 200, 300 kPa are associated in experiments with N_{ini} values equal to 100, 77 and 110, respectively – i.e., with no monotonic dependence of N_{ini} on p_{in} (and arguably with an influence of specimen preparation). Overall, the proposed SANISAND-MS formulation shows good ability to predict the impact of p_{in} both in terms of pore pressure build-up and strain accumulation with the upgraded formulation performing better than its previous version.

Influence of cyclic amplitude ratio The reference experimental data show that higher values of the cyclic amplitude stress ratio ($\eta_{ampl} = q_{ampl}/p_{in}$) result in faster triggering of liquefaction (i.e., lower N_{ini}) – see Fig.12a and Fig.12e. Both SANISAND-MS versions prove sensitive to this effect (see Fig.12b and Fig.12e). However, while Liu et al. (2019)'s formulation largely underestimates N_{ini} for $\eta_{ampl} = 0.2$ and 0.25, the upgraded model predicts accurate N_{ini} values in all considered cases. This confirms the effectiveness of the new hardening modulus definition in Eq.16. Further, the upgraded formulation captures well the axial strain accumulation, both on positive and negative sides (compare Fig.12c and Fig.12d).

Influence of initial relative density Wichtmann and Triantafyllidis (2016)'s data also confirm the expectation that, under given conditions, the effective mean pressure vanishes faster at lower initial relative density (see stress paths in Fig.13a and Fig.13e). Both SANISAND-MS versions succeed also in this respect (Fig.13b and Fig.13e). Nonetheless, the new formulation improves quantitative pore pressure predictions owing to the new material parameter w_2, which scales cyclic amplitude effects with respect to the void ratio (see Eq.16 and Fig.9) – compare experimental data and upgraded model predictions in Figs. 13a to 13b). The new model, however, seems to reproduce the influence on strain accumulation of the initial relative density (Figs.13c to 13d) less accurately than of other input factors (Figs.11 - 12).

Response of anisotropically consolidated sand

SANISAND-MS was further challenged to reproduce the undrained response of anisotropically consolidated sand specimens. Useful insight in this respect can be obtained from the comparison in Fig.14 between effective stress paths from experimental results (Wichtmann and Triantafyllidis 2016) and SANISAND-MS simulations. In particular, cases with cyclic stress amplitude ratio ($\eta_{ampl} = q_{ampl}/p_{in}$) smaller or larger than the initial average stress ratio ($\eta_{ave} = q_{ave}/p_{in}$) were considered in both experiments and simulations – Figs.14a, 14b. Fig.14 suggests that, when $\eta_{ampl} < \eta_{ave}$ (i.e., with no compression-to-extension reversals in terms of current cyclic stress ratio, Fig.14a), effective stress paths evolve towards steady loops after a few loading cycles – with no liquefaction triggering ($u^{acc}/p_{in} < 1$). This occurrence corresponds with the attainment of a pore pressure plateau in $u^{acc}/p_{in} - N$ plots (Fig.14c). Further, the characteristic butterfly shape of the steady stress path is well captured for $\eta_{ampl} > \eta_{ave}$ (see Fig.14b). When compared to laboratory data, SANISAND-MS simulations reproduce quite well such experimental evidence, including reasonable timing of effective mean pressure reduction against the number of cycles (Fig.14c), especially for $\eta_{ampl} > \eta_{ave}$.

Influence of drained cyclic pre-loading

It is well-known that previous loading history affects the hydro-mechanical response of sands to undrained cyclic loading, including their susceptibility to liquefaction. In this section the impact of drained cyclic pre-loading on subsequent undrained pore pressure build-up is explored. To this end, results from a different experimental database were considered. Fig.15 shows SANISAND-MS simulation results for the quartz sand tested by Wichtmann (2005) (D_{50} = 0.55 mm, D_{10} = 0.29 mm, $C_u = D_{60}/D_{10} = 1.8$, $e_{max} = 0.874$, $e_{min} = 0.577$), corresponding with p_{in} = 100 kPa, $e_{in} = 0.684$, undrained cyclic stress amplitude q^{pre}_{ampl} = 45 kPa. The model parameters calibrated for this second sand are reported in Table 3. Monotonic parameters and μ_0 (i.e., from G_0 to μ_0 in Table 3) coincide with those calibrated by Liu et al. (2018) and Liu et al. (2019), while the aforementioned default values $w_1 = 2$ and $w_2 = 0$ were assumed; β_1, β_2, k and ζ were calibrated against the deviatoric stress-axial strain response from only one stress-controlled triaxial test at constant cyclic amplitude.

Upgraded SANISAND-MS simulations were carried out for three different cases: (1) without drained pre-loading cycles; (2) with 10 drained pre-cycles of amplitude q^{pre}_{ampl} = 30 kPa, followed by undrained cyclic loading; (3) with 10 drained pre-cycles of amplitude q^{pre}_{ampl} = 50 kPa, followed by undrained cyclic loading. It is generally observed that drained cyclic pre-loading under the phase-transformation line tends to delay the onset of liquefaction (i.e., to increase N_{ini}, see $q - p$ stress paths in Figs.15a–15c).

Simulation results in Fig.15d (red lines) are in very good agreement with experimental measurements (black lines) in terms of pore water pressure accumulation, and support the suitability of the adopted memory surface framework. In essence, applying drained cyclic pre-loading contributes to the “reinforcement” of sand fabric. This aspect is phenomenologically tracked by the model through the corresponding evolution of the memory surface size/location, and thus exploited to re-tune soil stiffness and dilatancy. The larger m^M, the higher the resistance to liquefaction, i.e., the larger N_{ini}. As highlighted in Fig. 15e, accurate simulation of effective stress paths enables to reliably predict the dependence of N_{ini} on the amplitude of drained pre-cycles. It is finally worth noting that the parent SANISAND04 model (Dafalias and Manzari 2004) would be practically insensitive to drained cyclic pre-loading, except for the effect of a slightly different void ratio at the beginning of undrained cycling.

CONCLUDING REMARKS

The memory-enhanced bounding surface model proposed by Liu et al. (2019), SANISAND-MS, was improved to reproduce essential features of the hydro-mechanical response of sands to undrained cyclic loading. The previous mathematical formulation was upgraded by: (i) modifying memory surface evolution laws to better reflect fabric effects at larger strains; (ii) enhancing the description of sand dilatancy through new terms accounting for fabric evolution history, and stress state/path; (iii) incorporating a deviatoric stress ratio term into the hardening modulus. While ready application to 3D boundary value problems was the main motivation of such effort, a few aspects of the proposed constitutive model will require further research in the near future, for instance to: (a) avoid discontinuities in the dilatancy formulation; (b) more flexibly model deviatoric strain accumulation during cyclic mobility, e.g., by allowing for strain saturation limits if observed in experimental data; (c) investigate the evolution of fabric history effects through varying drainage conditions.

The above modifications enabled substantial improvement of simulated pore pressure build-up and cyclic mobility, with sound sensitiveness to the main governing factors. After parameter calibration, the model was thoroughly validated against published results of undrained cyclic triaxial tests. Further qualitative insight into the expected effect of different loading conditions (e.g., under simple shear loading). The upgraded SANISAND-MS model confirmed the suitability of combining the memory surface concept with the well-established bounding surface plasticity framework.

APPENDIX A: UPGRADED SANISAND-MS CONSTITUTIVE EQUATIONS

FEATURE	EQUATION	PARAMETER
Elasticity	$G = G_0 p_{atm}(2.97 - e)^2/(1+e)\sqrt{p/p_{atm}}$ $K = 2(1+\nu)G/[3(1-2\nu)]$	G_0 dimensionless shear modulus ν Poisson ratio
Critical state line	$e_c = e_0 - \lambda_c (p_c/p_{atm})^{\xi}$	e_0 reference critical void ratio λ_c, ξ CSL shape parameters
Yield surface	$f = \sqrt{(\boldsymbol{s} - p\boldsymbol{\alpha}) : (\boldsymbol{s} - p\boldsymbol{\alpha})} - \sqrt{2/3}pm$	m yield locus opening parameter
Memory surface	$f^M = \sqrt{(\boldsymbol{s} - p\boldsymbol{\alpha}^M) : (\boldsymbol{s} - p\boldsymbol{\alpha}^M)} - \sqrt{2/3}pm^M$	
Plastic hardening	$d\boldsymbol{\alpha} = (2/3)\langle L \rangle h(\boldsymbol{\alpha}^b - \boldsymbol{\alpha})$ $\boldsymbol{\alpha}^b = \sqrt{2/3}\left[g(\theta)M\exp(-n^b\Psi) - m\right]\boldsymbol{n}$ $g(\theta) = 2c/[(1+c) - (1-c)\cos 3\theta]$ $L = (1/K_p)\partial f/\partial\boldsymbol{\sigma} : d\boldsymbol{\sigma}$ $K_p = (2/3)ph(\boldsymbol{\alpha}^b - \boldsymbol{\alpha}) : \boldsymbol{n}$ $\boldsymbol{n} = (\boldsymbol{r} - \boldsymbol{\alpha})/\sqrt{2/3}m$ $\Psi = e - e_c$ $h = \dfrac{b_0}{(\boldsymbol{\alpha} - \boldsymbol{\alpha}_{in}) : \boldsymbol{n}}\exp\left[\mu_0\left(\dfrac{p}{p_{atm}}\right)^{0.5}\left(\dfrac{b^M}{b_{ref}}\right)^{w_1}\dfrac{1}{\eta^{w_2}}\right]$ $b_0 = G_0 h_0(1 - c_h e)/\sqrt{p/p_{atm}}$ $b^M = (\boldsymbol{r}_{\alpha}^M - \boldsymbol{\alpha}) : \boldsymbol{n}$ $b_{ref} = (\boldsymbol{\alpha}^b - \tilde{\boldsymbol{\alpha}}^b) : \boldsymbol{n}$ $\tilde{\boldsymbol{\alpha}}^b = -\sqrt{2/3}[g(\theta+\pi)M\exp(-n^b\Psi) - m]\boldsymbol{n}$ $\boldsymbol{r}_{\alpha}^M = \boldsymbol{\alpha}^M + \sqrt{2/3}(m^M - m)\boldsymbol{n}$	n^b bounding surface evolution parameter M critical stress ratio c extension-to-compression strength ratio μ_0, w_1 memory-hardening parameters w_2 cyclic stress ratio parameter h_0, c_h hardening parameters
Memory surface evolution	$dm^M = dm_+^M + dm_-^M$ $dm_+^M = \sqrt{3/2}d\boldsymbol{\alpha}^M : \boldsymbol{n}$ $dm_-^M = -(m^M/\zeta)f_{shr}\langle b_r^b\rangle m_+^M\langle -d\varepsilon_{vol}^p\rangle$ $F = \ln[1 + \lvert m_-^M\rvert/(\lvert m_-^M\rvert + \lvert m_+^M\rvert)^{0.5}]$ $b_r^b = (\boldsymbol{\alpha}^b - \boldsymbol{\alpha}) : \boldsymbol{n}$ $d\boldsymbol{\alpha}^M = (2/3)\langle L^M\rangle h^M(\boldsymbol{\alpha}^b - \boldsymbol{r}_{\alpha}^M)$ $h^M = \dfrac{1}{2}\left[\dfrac{b_0}{(\boldsymbol{r}_{\alpha}^M - \boldsymbol{\alpha}_{in}) : \boldsymbol{n}} + \sqrt{\dfrac{3}{2}}\dfrac{m^M m_+^M\langle b_r^b\rangle f_{shr}\langle -D\rangle}{\zeta(\boldsymbol{\alpha}^b - \boldsymbol{r}_{\alpha}^M) : \boldsymbol{n}}\right]$	ζ memory surface shrinkage parameter
Deviatoric plastic flow	$d\boldsymbol{e}^p = \langle L\rangle\boldsymbol{R}' = \langle L\rangle\left\{B\boldsymbol{n} - C\left[\boldsymbol{n}^2 - (1/3)\boldsymbol{I}\right]\right\}$ $B = 1 + 3(1-c)/(2c)g(\theta)\cos 3\theta$ $C = 3\sqrt{3/2}(1-c)/cg(\theta)$	
Volumetric plastic flow	$d\varepsilon_{vol}^p = \langle L\rangle D$ $d = (\boldsymbol{\alpha}^d - \boldsymbol{\alpha}) : \boldsymbol{n}$ $D = A_d d$ $A_d = A_0$ (for $d \geq 0$ and $\tilde{b}_d^M \leq 0$) $A_d = A_0\exp\left[\beta_1 F\left(\dfrac{p}{p_{max}}\right)^{0.5}\right]g^k(\theta)$ (for $d \geq 0$ and $\tilde{b}_d^M > 0$) $A_d = A_0\exp\left[\beta_2 F\left(1 - \left(\dfrac{p}{p_{max}}\right)^{0.5}\right)\dfrac{d}{\lVert\boldsymbol{\alpha}^c\rVert}\right]\dfrac{1}{g(\theta)}$ (for $d < 0$) $\boldsymbol{\alpha}^c = \sqrt{2/3}(g(\theta)M - m)\boldsymbol{n}$ $\boldsymbol{\alpha}^d = \sqrt{2/3}\left[g(\theta)M\exp(n^d\Psi) - m\right]\boldsymbol{n}$ $\tilde{b}_d^M = (\tilde{\boldsymbol{\alpha}}^d - \tilde{\boldsymbol{r}}_{\alpha}^M) : \boldsymbol{n}$ $\tilde{\boldsymbol{\alpha}}^d = -\sqrt{2/3}\left[g(\theta+\pi)M\exp(n^d\Psi) - m\right]\boldsymbol{n}$	A_0 'intrinsic' dilatancy parameter β_1 dilatancy parameter k dilatancy parameter β_2 dilatancy parameter n^d dilatancy surface evolution parameter

DATA AVAILABILITY STATEMENT

Some or all data, models, or code that support the findings of this study are available from the corresponding author upon reasonable request.

ACKNOWLEDGEMENTS

The authors wish to acknowledge the China Scholarship Council (CSC) and the Geo-Engineering Section of Delft University of Technology for financial support of the first author. The constructive feedback of two anonymous reviewers is also highly appreciated.

REFERENCES

Andersen, K. H. (2009). "Bearing capacity under cyclic loading offshore, along the coast, and on land. the 21st Bjerrum lecture presented in Oslo, 23 november 2007." *Canadian Geotechnical Journal*, 46(5), 513–535.

Arulmoli, K., Muraleetharan, K., Hossain, M., and Fruth, L. (1992). "VELACS: Verification of liquefaction analysis by centrifuge studies." *Laboratory Testing Program, Soil Data Rep. No. 90*, 562.

Barrero, A. R., Taiebat, M., and Dafalias, Y. F. (2019). "Modeling cyclic shearing of sands in the semifluidized state." *International Journal for Numerical and Analytical Methods in Geomechanics*.

Been, K. and Jefferies, M. G. (1985). "A state parameter for sands." *Géotechnique*, 35(2), 99–112.

Berrill, J. and Davis, R. (1985). "Energy dissipation and seismic liquefaction of sands: revised model." *Soils and Foundations*, 25(2), 106–118.

Boulanger, R. and Ziotopoulou, K. (2013). "Formulation of a sand plasticity plane-strain model for earthquake engineering applications." *Soil Dynamics and Earthquake Engineering*, 53, 254–267.

Chiaradonna, A., Tropeano, G., D'Onofrio, A., and Silvestri, F. (2018). "Development of a simplified model for pore water pressure build-up induced by cyclic loading." *Bulletin of Earthquake Engineering*, 1–26.

Corti, R., Diambra, A., Muir Wood, D., Escribano, D. E., and Nash, D. F. (2016). "Memory surface hardening model for granular soils under repeated loading conditions." *Journal of Engineering Mechanics*, 04016102.

Dafalias, Y. and Popov, E. (1975). “A model of nonlinearly hardening materials for complex loading.” *Acta mechanica*, 21(3), 173–192.

Dafalias, Y. and Taiebat, M. (2016). “SANISAND-Z: zero elastic range sand plasticity model.” *Géotechnique*, 66(12), 999–1013.

Dafalias, Y. F. and Manzari, M. T. (2004). “Simple plasticity sand model accounting for fabric change effects.” *Journal of Engineering mechanics*, 130(6), 622–634.

Dobry, R., Pierce, W., Dyvik, R., Thomas, G., and Ladd, R. (1985). “Pore pressure model for cyclic straining of sand.” *Rensselaer Polytechnic Institute, Troy, New York*.

Elgamal, A., Yang, Z., Parra, E., and Ragheb, A. (2003). “Modeling of cyclic mobility in saturated cohesionless soils.” *International Journal of Plasticity*, 19(6), 883–905.

Houlsby, G., Abadie, C., Beuckelaers, W., and Byrne, B. (2017). “A model for nonlinear hysteretic and ratcheting behaviour.” *International Journal of Solids and Structures*, 120, 67–80.

Houlsby, G. and Mortara, G. (2004). “A continuous hyperplasticity model for sands under cyclic loading.” *Cyclic Behaviour of Soils and Liquefaction Phenomena: Proceedings of the International Conference, Bochum, Germany, 31 March-2 April 2004*, CRC Press, 21.

Idriss, I. and Boulanger, R. (2006). “Semi-empirical procedures for evaluating liquefaction potential during earthquakes.” *Soil Dynamics and Earthquake Engineering*, 26(2-4), 115–130.

Ishihara, K. (1993). “Liquefaction and flow failure during earthquakes.” *Géotechnique*, 43(3), 351–451.

Ivšić, T. (2006). “A model for presentation of seismic pore water pressures.” *Soil Dynamics and Earthquake Engineering*, 26(2-4), 191–199.

Kementzetzidis, E., Corciulo, S., Versteijlen, W. G., and Pisanò, F. (2019). “Geotechnical aspects of offshore wind turbine dynamics from 3D non-linear soil-structure simulations.” *Soil Dynamics and Earthquake Engineering*, 120, 181–199.

Khosravifar, A., Elgamal, A., Lu, J., and Li, J. (2018). “A 3D model for earthquake-induced liquefaction triggering and post-liquefaction response.” *Soil Dynamics and Earthquake Engineering*, 110, 43–52.

Kokusho, T. (2013). "Liquefaction potential evaluations: energy-based method versus stress-based method." *Canadian Geotechnical Journal*, 50(10), 1088–1099.

Li, X. and Dafalias, Y. F. (2000). "Dilatancy for cohesionless soils." *Geotéchnique*, 50(4), 449–460.

Liu, H. Y., Abell, J. A., Diambra, A., and Pisanò, F. (2019). "Modelling the cyclic ratcheting of sands through memory- enhanced bounding surface plasticity." *Géotechnique*, 69(9), 783–800.

Liu, H. Y. and Pisanò, F. (2019). "Prediction of oedometer terminal densities through a memory-enhanced cyclic model for sand." *Géotechnique Letters*, 9(2), 81–88.

Liu, H. Y., Zygounas, F., Diambra, A., and Pisanò, F. (2018). "Enhanced plasticity modelling of high-cyclic ratcheting and pore pressure accumulation in sands." *Numerical Methods in Geotechnical Engineering IX, Volume 1: Proceedings of the 9th European Conference on Numerical Methods in Geotechnical Engineering (NUMGE 2018), June 25-27, 2018, Porto, Portugal*, CRC Press, 87.

Maleki, M., Cambou, B., and Dubujet, P. (2009). "Development in modeling cyclic loading of sands based on kinematic hardening." *International journal for numerical and analytical methods in geomechanics*, 33(14), 1641–1658.

Manzari, M. T. and Dafalias, Y. F. (1997). "A critical state two-surface plasticity model for sands." *Géotechnique*, 47(2), 255–272.

Nemat-Nasser, S. and Tobita, Y. (1982). "Influence of fabric on liquefaction and densification potential of cohesionless sand." *Mechanics of Materials*, 1(1), 43–62.

Papadimitriou, A. G. and Bouckovalas, G. D. (2002). "Plasticity model for sand under small and large cyclic strains: a multiaxial formulation." *Soil Dynamics and Earthquake Engineering*, 22(3), 191–204.

Petalas, A. L., Dafalias, Y. F., and Papadimitriou, A. G. (2019). "Sanisand-fn: An evolving fabric-based sand model accounting for stress principal axes rotation." *International Journal for Numerical and Analytical Methods in Geomechanics*, 43(1), 97–123.

Pisanò, F. (2019). "Input of advanced geotechnical modelling to the design of offshore wind turbine foundations." *Proceedings of the 17th European Conference on Soil Mechanics and Geotechnical*

Engineering (ECSMGE 20198), September 1-6, 2019, Reykjavik, Iceland.

Pisanò, F. and Jeremić, B. (2014). "Simulating stiffness degradation and damping in soils via a simple visco-elastic–plastic model." *Soil Dynamics and Earthquake Engineering*, 63, 98–109.

Prévost, J. H. (1985). "A simple plasticity theory for frictional cohesionless soils." *International Journal of Soil Dynamics and Earthquake Engineering*, 4(1), 9–17.

Roten, D., Fäh, D., and Bonilla, L. F. (2013). "High-frequency ground motion amplification during the 2011 tohoku earthquake explained by soil dilatancy." *Geophysical Journal International*, 193(2), 898–904.

Seed, B. and Lee, K. L. (1966). "Liquefaction of saturated sands during cyclic loading." *Journal of Soil Mechanics & Foundations Div*, 92(ASCE# 4972 Proceeding).

Seed, H. B. and Rahman, M. (1978). "Wave-induced pore pressure in relation to ocean floor stability of cohesionless soils." *Marine Georesources & Geotechnology*, 3(2), 123–150.

Stallebrass, S. and Taylor, R. (1997). "The development and evaluation of a constitutive model for the prediction of ground movements in overconsolidatcd clay." *Géotechnique*, 47, 235–253.

Vaid, Y. and Thomas, J. (1995). "Liquefaction and postliquefaction behavior of sand." *Journal of Geotechnical Engineering*, 121(2), 163–173.

Wang, G. and Wei, J. (2016). "Microstructure evolution of granular soils in cyclic mobility and post-liquefaction process." *Granular Matter*, 18(3), 51.

Wang, R., Fu, P., Zhang, J.-M., and Dafalias, Y. F. (2016). "Dem study of fabric features governing undrained post-liquefaction shear deformation of sand." *Acta Geotechnica*, 11(6), 1321–1337.

Wichtmann, T. (2005). "Explicit accumulation model for non-cohesive soils under cyclic loading." Ph.D. thesis, Inst. für Grundbau und Bodenmechanik Bochum University, Germany.

Wichtmann, T. and Triantafyllidis, T. (2016). "An experimental database for the development, calibration and verification of constitutive models for sand with focus to cyclic loading: part iitests with strain cycles and combined loading." *Acta Geotechnica*, 11(4), 763–774.

Yimsiri, S. and Soga, K. (2010). "Dem analysis of soil fabric effects on behaviour of sand." *Géotechnique*, 60(6), 483.

Youd, T. L. (1993). “Liquefaction-induced lateral spread displacement.” *Report no.*, Naval Civil Engineering Lab, Port Hueneme (CA).

Zhang, J.-M. and Wang, G. (2012). “Large post-liquefaction deformation of sand, part i: physical mechanism, constitutive description and numerical algorithm.” *Acta Geotechnica*, 7(2), 69–113.

Ziotopoulou, K. and Boulanger, R. (2016). “Plasticity modeling of liquefaction effects under sloping ground and irregular cyclic loading conditions.” *Soil Dynamics and Earthquake Engineering*, 84, 269–283.

List of Tables

TABLE 1. Parameters of Liu et al. (2019) model for the Karlsruhe fine sand tested by Wichtmann & Triantafyllidis (2016)

FEATURE	PARAMETER	VALUE
Elasticity	G_0	95
	ν	0.05
Critical state	M	1.35
	c	0.81
	λ_c	0.055
	e_0	1.035
	ξ	0.36
Yield	m	0.01
Plastic Modulus	h_0	7.6
	c_h	0.97
	n^b	1.2
Dilatancy	A_0	0.74
	n^d	1.79
Memory surface	μ_0	82
	ζ	0.0005
	β	4

TABLE 2. Upgraded SANISAND-MS parameters for the Karlsruhe fine sand tested by Wichtmann & Triantafyllidis (2016)

FEATURE	PARAMETER	VALUE
Elasticity	G_0	95
	ν	0.05
Critical state	M	1.35
	c	0.81
	λ_c	0.055
	e_0	1.035
	ξ	0.36
Yield	m	0.01
Plastic Modulus	h_0	7.6
	c_h	0.97
	n^b	1.2
Dilatancy	A_0	0.74
	n^d	1.79
	β_1	4
	β_2	3.2
	k	2
Memory surface	μ_0	65
	ζ	0.0005
	w_1	2.5
	w_2	1.5

TABLE 3. Upgraded SANISAND-MS parameters for the quartz sand tested by Wichtmann (2005)

FEATURE	PARAMETER	VALUE
Elasticity	G_0	110
	ν	0.05
Critical state	M	1.27
	c	0.712
	λ_c	0.049
	e_0	0.845
	ξ	0.27
Yield	m	0.01
Plastic Modulus	h_0	5.95
	c_h	1.01
	n^b	2
Dilatancy	A_0	1.06
	n^d	1.17
	β_1	1.9
	β_2	2.1
	k	1
Memory surface	μ_0	260
	ζ	0.0001
	w_1	2
	w_2	0

List of Figures

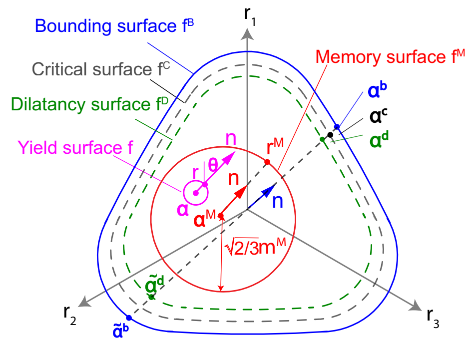

Fig. 1. SANISAND-MS loci in the deviatoric stress ratio plane.

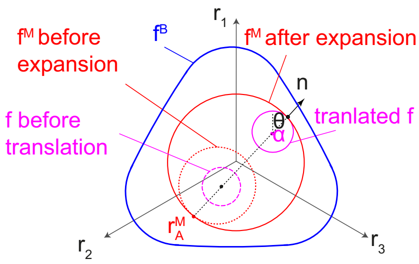

(a) Memory surface expansion and translation

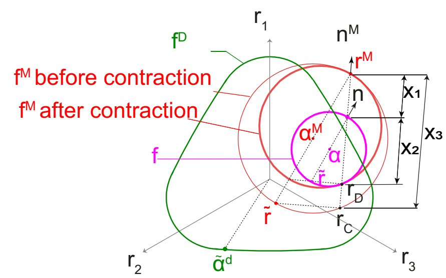

(b) Memory surface contraction

Fig. 2. Evolution of the memory surface

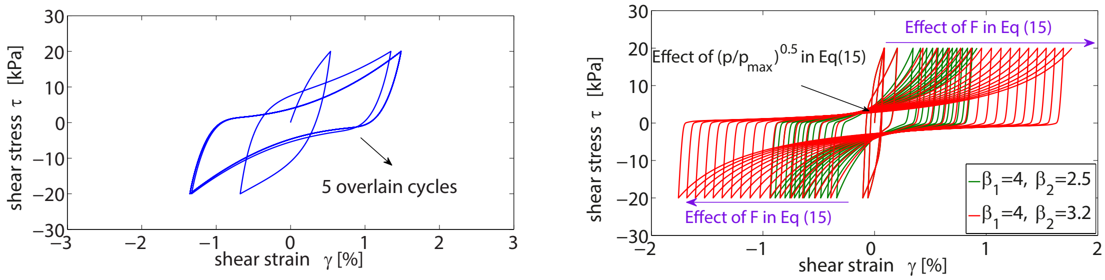

(a) Liu et al. (2019)'s formulation

(b) upgraded formulation

Fig. 3. Cyclic DSS simulations via SANISAND-MS. Simulation conditions: $e_{in} = 0.812$ (initial void ratio), $\sigma_v = 100$ kPa (effective vertical stress), $\tau_{ampl} = \pm 20$ kPa (cyclic shear stress amplitude); cyclic parameters in the upgraded model: $\mu_0 = 65$, $\zeta = 0.0003$, $w_1 = 2.5$, $w_2 = 1.5$, $k = 2$.

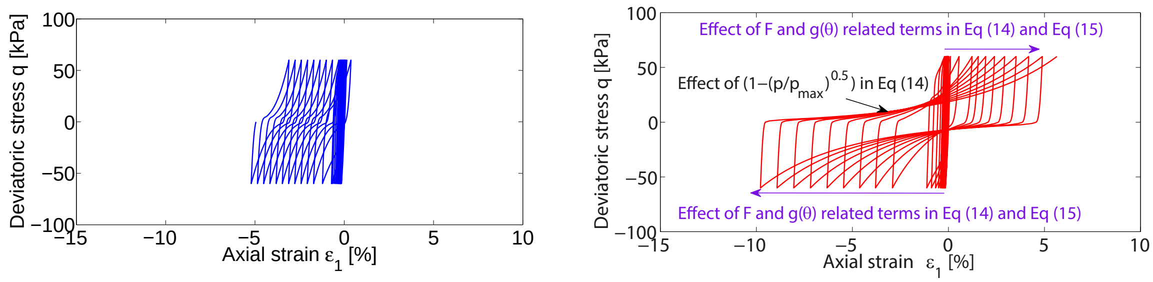

(a) Liu et al. (2019)'s formulation

(b) upgraded formulation

Fig. 4. Cyclic triaxial simulations on isotropically consolidated sand via SANISAND-MS. Simulation settings: $e_{in} = 0.825$, $p_{in} = 100$ kPa, $q_{ampl} = 30$ kPa. Cyclic parameters in the upgraded model: $\mu_0 = 65$, $\zeta = 0.0003$, $w_1 = 2.5$, $w_2 = 1.5$, $\beta_1 = 4.0$, $\beta_2 = 3.2$, $k = 2$.

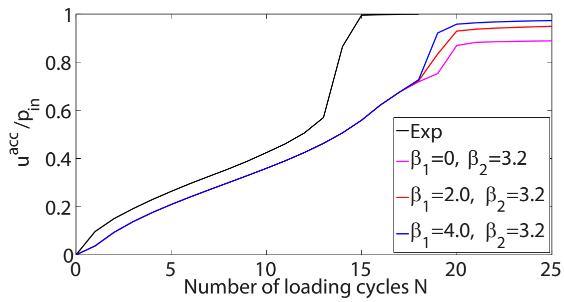

Fig. 5. Calibration of β_1. Test/simulation settings and cyclic parameters are as in Fig.4b (Data from Wichtmann and Triantafyllidis 2016).

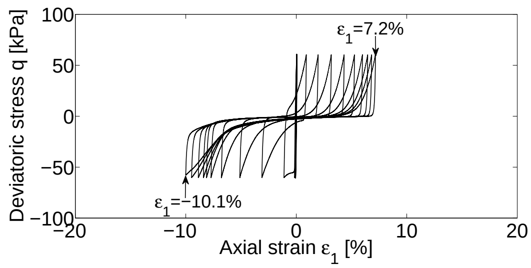

(**a**) triaxial test (Data from Wichtmann and Triantafyllidis 2016)

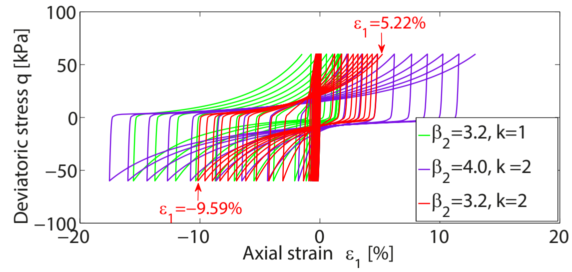

(**b**) upgraded SANISAND-MS simulations

Fig. 6. Calibration of β_2 and k. Test/simulation settings: $e_{in} = 0.8$, $p_{in} = 200$ kPa, $q_{ampl} = 200$ kPa. Cyclic parameters in the upgraded model: $\mu_0 = 65$, $\zeta = 0.0003$, $w_1 = 2.5$, $w_2 = 1.5$, $\beta_1 = 4.0$. Number of loading cycles after initial liquefaction $N = 10$.

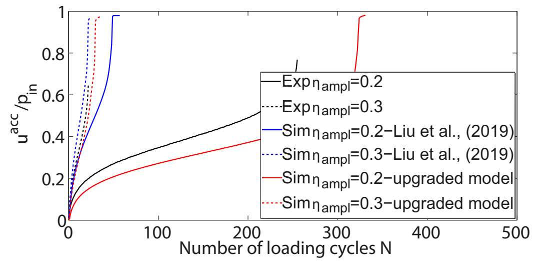

Fig. 7. Performance of previous and upgraded SANISAND-MS (model parameters in Table 1 and Table 2, respectively) on pore pressure accumulation in isotropically consolidated sand under varying stress amplitude ratios η_{ampl}. Test/simulation settings: performed with an initial drained loading cycle, p_{in} = 300 kPa, e_{in} = 0.846 when η_{ampl} = 0.2; e_{in} = 0.816 when η_{ampl} = 0.3 (Data from Wichtmann and Triantafyllidis 2016).

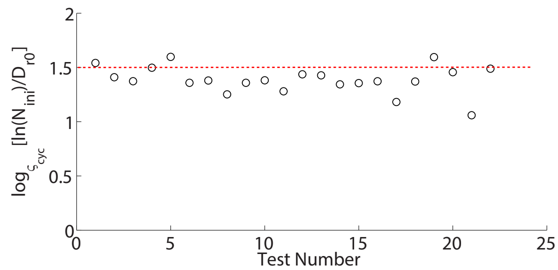

Fig. 8. Calibration of w_2 based on the results of undrained cyclic triaxial tests on isotropically consolidated sand (Data from Wichtmann and Triantafyllidis 2016.

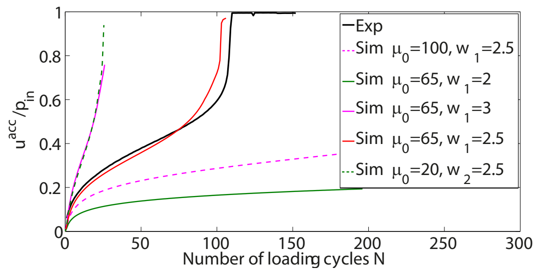

Fig. 9. Calibration of w_1 and μ_0. Test/simulation settings: performed with an initial drained loading cycle, $e_{in} = 0.808$, $p_{in} = 300$ kPa, $\eta_{ampl} = 0.25$. Cyclic parameters in the upgraded model: $\beta_1 = 4.0$, $\beta_2 = 3.2$, $w_2 = 1.5$, $k = 2$, $\zeta = 0.0003$.

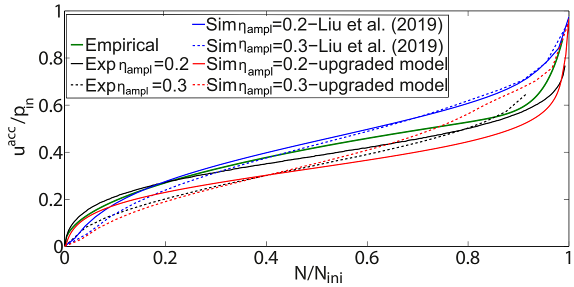

Fig. 10. Pore pressure accumulation curves. Same test/simulation settings as in Fig.7. Comparison among experimental data (Wichtmann & Triantafyllidis, 2016), empirical fit (Chiaradonna et al., 2018) and SANISAND-MS simulations.

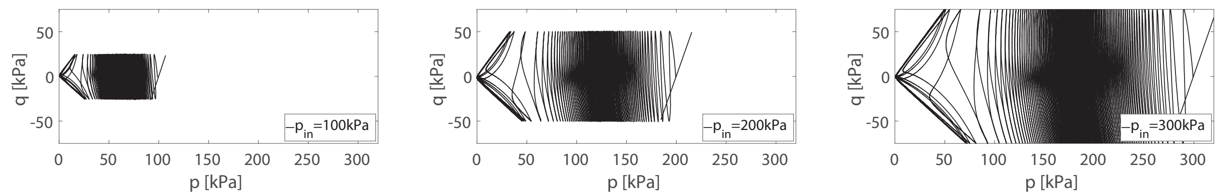

(a) Experimental results: q-p response with, p_{in}=100, 200, 300 kPa

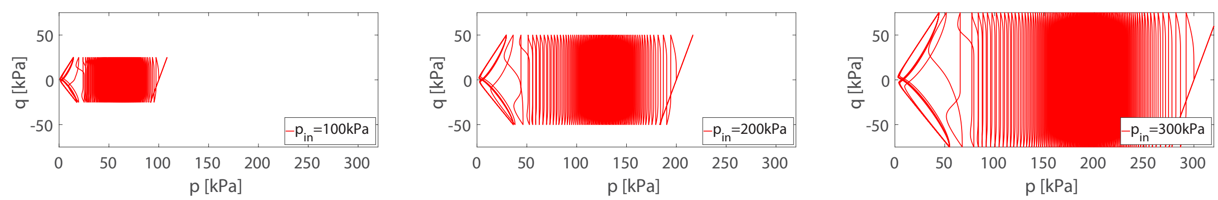

(b) Upgraded SANISAND-MS results: q-p response with, p_{in}=100, 200, 300 kPa

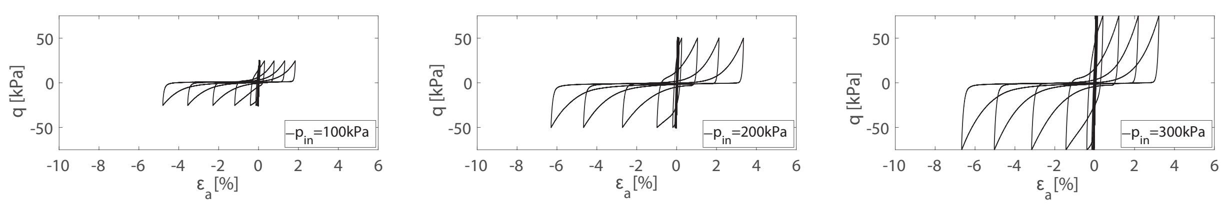

(c) Experimental results: q-ε_a response with, p_{in}=100, 200, 300 kPa

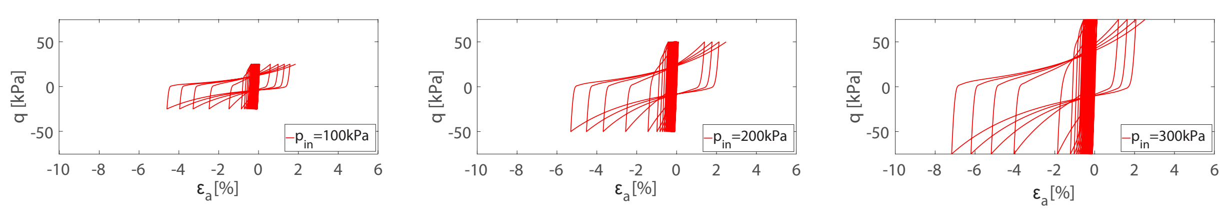

(d) Upgraded SANISAND-MS results: q-ε_a response for p_{in}=100, 200, 300 kPa

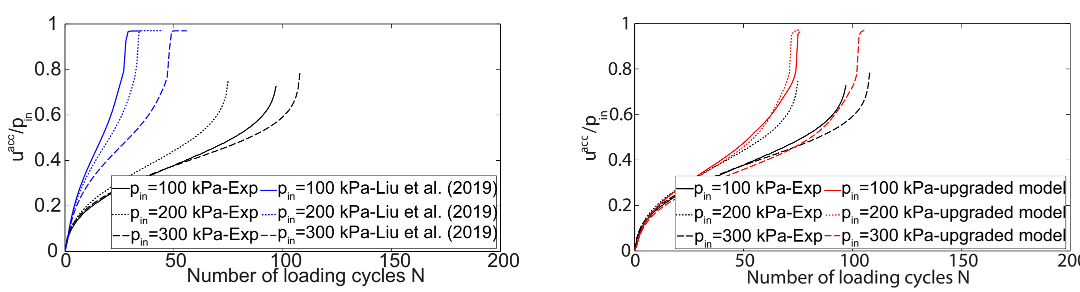

(e) SANISAND-MS vs experimental results: pore pressure accumulation predictions from Liu et al. (2019)'s formulation and upgraded model

Fig. 11. Influence of initial effective mean pressure on pore pressure accumulation in isotropically consolidated sand. Test/simulation settings: performed with an initial drained loading cycle, p_{in} = 100 kPa (e_{in} = 0.798), 200 kPa (e_{in} = 0.813) and 300 kPa (e_{in} = 0.808), η_{ampl} = 0.25. Comparison between experimental data (Wichtmann & Triantafyllidis, 2016) and SANISAND-MS simulations.

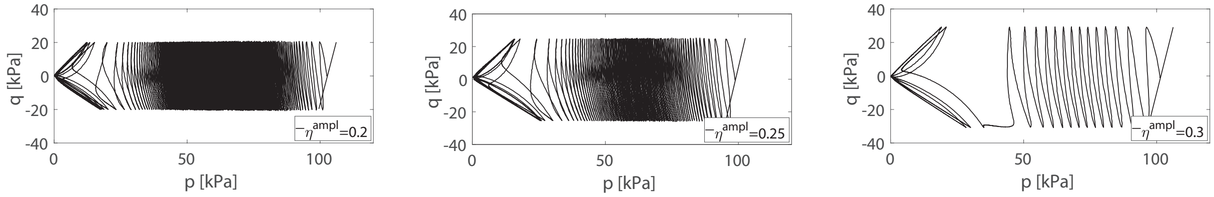

(a) Experimental results: q-p response for η^{ampl}=0.2, 0.25, 0.3

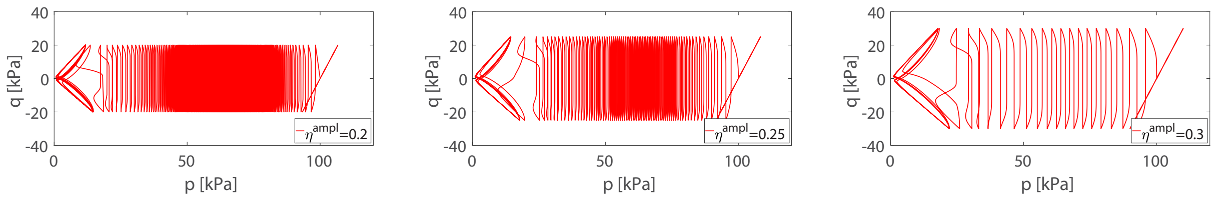

(b) Upgraded SANISAND-MS results: q-p response for η^{ampl}=0.2, 0.25, 0.3

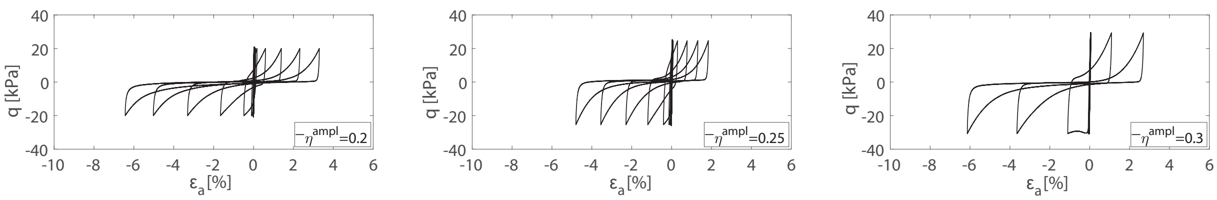

(c) Experimental results: q-ε_a response for η^{ampl}=0.2, 0.25, 0.3

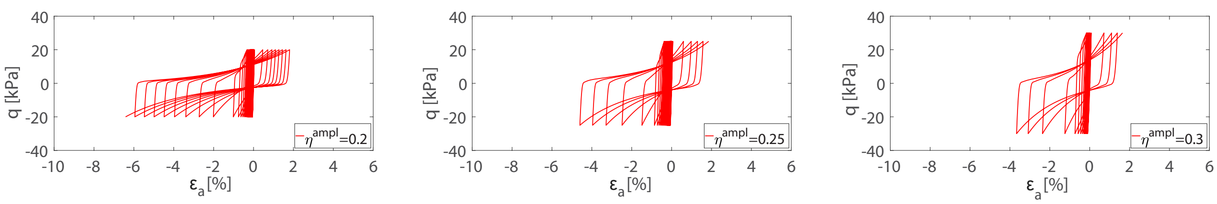

(d) Upgraded SANISAND-MS results: q-ε_a response for η^{ampl}=0.2, 0.25, 0.3

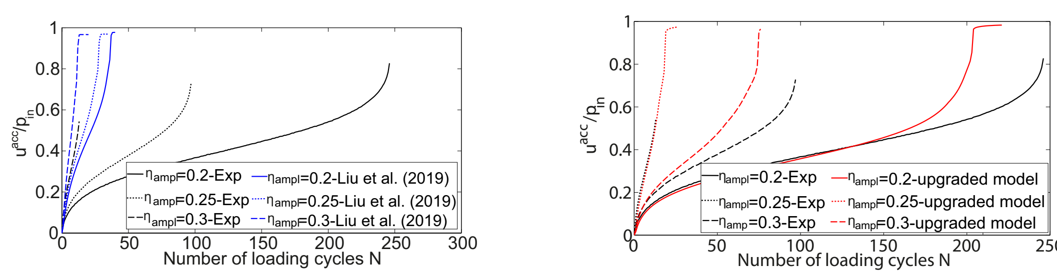

(e) SANISAND-MS vs experimental results: pore pressure accumulation predictions from Liu et al. (2019)'s formulation and upgraded model

Fig. 12. Influence of cyclic amplitude ratio η_{ampl} on undrained cyclic behaviour of isotropically consolidated sand. Test/simulation settings: performed with an initial drained loading cycle, e_{in} = 0.821, 0.798, 0.825 for η_{ampl} = 0.2, 0.25 and 0.3; p_{in} = 100 kPa. Comparison between experimental data (Wichtmann & Triantafyllidis, 2016) and SANISAND-MS simulations.

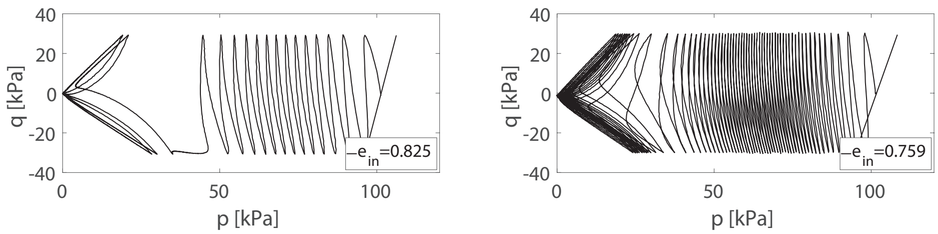

(a) Experimental results: q-p response for e_{in} =0.825 and e_{in} =0.759

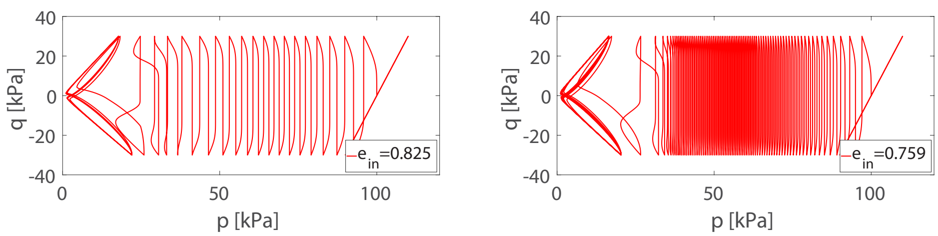

(b) Upgraded SANISAND-MS results: q-p response for e_{in} =0.825 and e_{in} =0.759

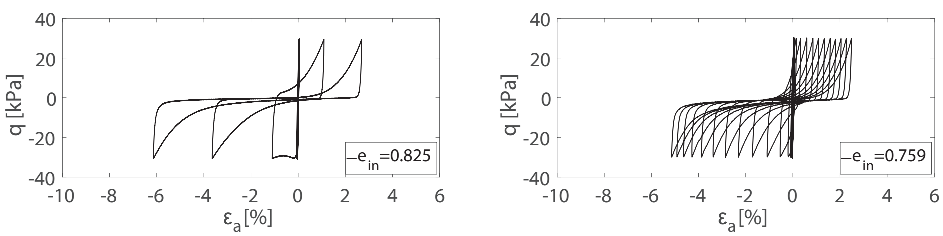

(c) Experimental results: q-ε_a response for e_{in} =0.825 and e_{in} =0.759

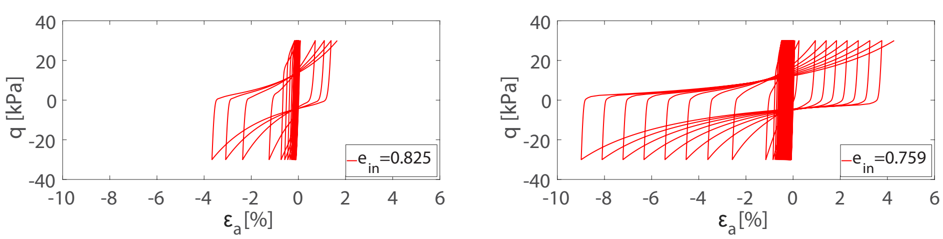

(d) Upgraded SANISAND-MS results: q-ε_a response for e_{in} =0.825 and e_{in} =0.759

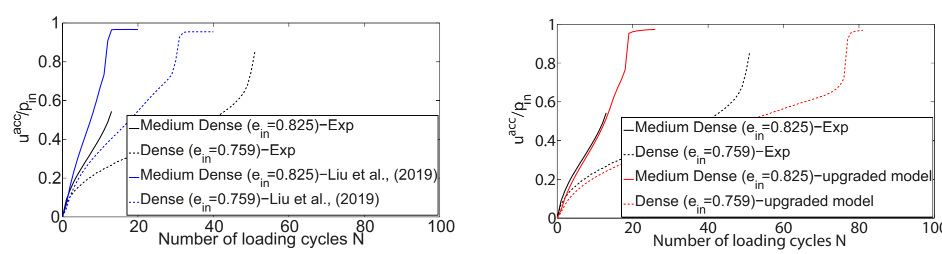

(e) SANISAND-MS vs experimental results: pore pressure accumulation predictions from Liu et al. (2019)'s formulation and upgraded model

Fig. 13. Influence of initial relative density on pore pressure accumulation in isotropically consolidated sand. Test/simulation settings: performed with an initial drained loading cycle, medium-dense sand (e_{in} = 0.825) and dense sand (e_{in} = 0.759), p_{in} = 100 kPa, η_{ampl} = 0.3. Comparison between experimental data (Wichtmann & Triantafyllidis, 2016) and SANISAND-MS simulations.

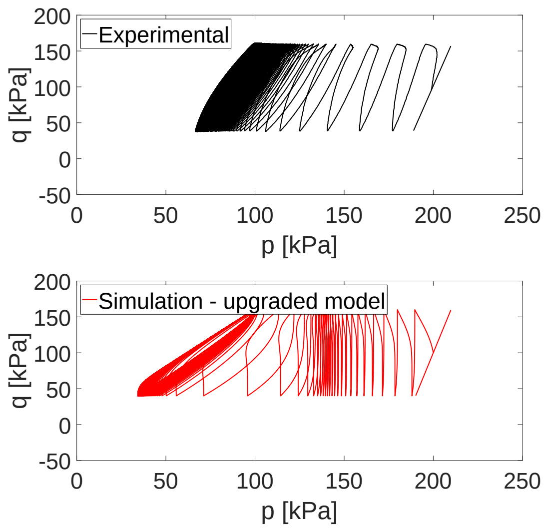

(a) $\eta_{ampl} = 0.3 < \eta_{ave} = 0.5$, $e_{in} = 0.838$

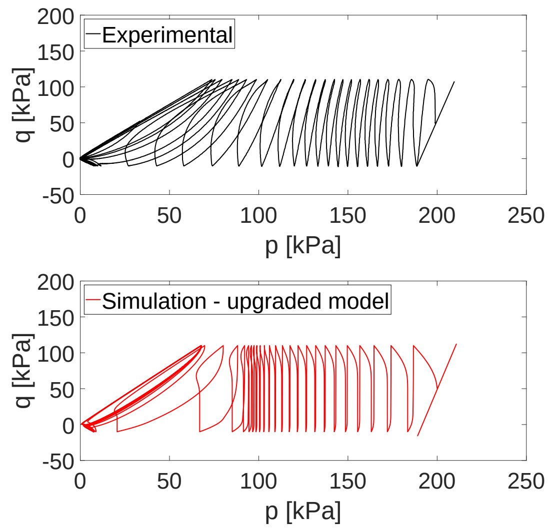

(b) $\eta_{ampl} = 0.3 > \eta_{ave} = 0.25$, $e_{in} = 0.843$

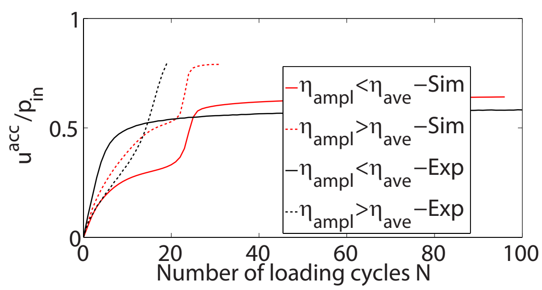

(c) pore pressure generation

Fig. 14. Relative effect of cyclic stress amplitude ratio η_{ampl} and initial average stress ratio η_{ave} on the undrained effective stress path in anisotropically consolidated sand. Test/simulation settings: performed with an initial drained loading cycle, p_{in} = 200 kPa, q_{ampl} = 60 kPa (Data from Wichtmann and Triantafyllidis 2016).

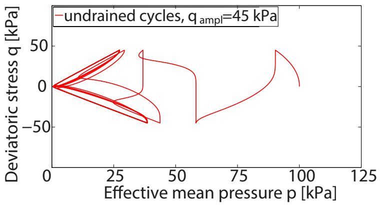

(a) without drained pre-cycles

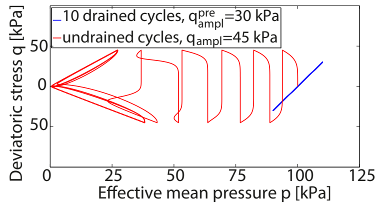

(b) 10 pre-cycles, $q^{pre}_{ampl} = 30kPa$

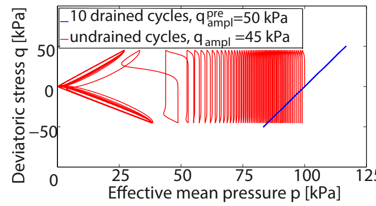

(c) 10 pre-cycles, $q^{pre}_{ampl} = 50kPa$

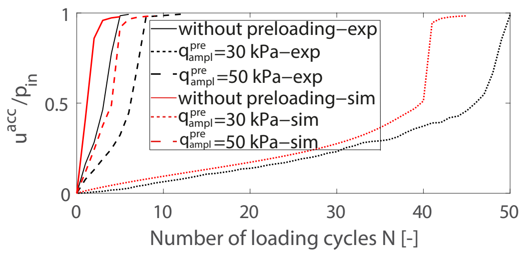

(d) pore pressure build-up curve

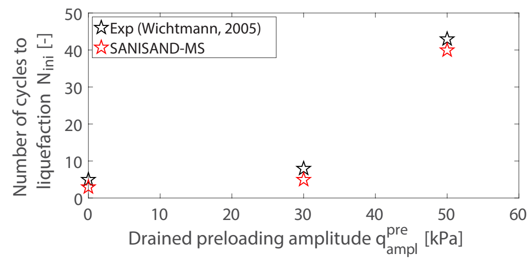

(e) Dependence of N_{ini} on q^{pre}_{ampl}

Fig. 15. Effect of drained cyclic pre-loading on the undrained cyclic triaxial response of the quartz sand (Wichtmann, 2005) – isotropically consolidated sand. Test/simulation settings: $e_{in} = 0.678$, $p_{in} = 100$ kPa, cyclic stress amplitude during undrained loading: $q_{ampl} = 45$ kPa.